

BS-LDM: Effective Bone Suppression in High-Resolution Chest X-Ray Images with Conditional Latent Diffusion Models

Yifei Sun¹, Zhanghao Chen¹, Hao Zheng¹, Ruiquan Ge¹, Jin Liu²
Wenwen Min³, Ahmed Elazab⁴, Xiang Wan⁵, Changmiao Wang^{5*}

Hangzhou Dianzi University¹, Central South University², Yunnan University³
Shenzhen University⁴, Shenzhen Research Institute of Big Data⁵

{22320232, bennychan, 22320210, gespring}@hdu.edu.cn, liujin06@csu.edu.cn, minwenwen@ynu.edu.cn
ahmedelazab@szu.edu.cn, wanxiang@sribd.cn, cmwangalbert@gmail.com

Abstract

The interference of overlapping bones and pulmonary structures can reduce the effectiveness of Chest X-ray (CXR) examinations. Bone suppression techniques have been developed to improve diagnostic accuracy. Dual-energy subtraction (DES) imaging, a common method for bone suppression, is costly and exposes patients to higher radiation levels. Deep learning-based image generation methods have been proposed as alternatives, however, they often fail to produce high-quality and high-resolution images, resulting in the loss of critical lesion information and texture details. To address these issues, in this paper, we introduce an end-to-end framework for bone suppression in high-resolution CXR images (1024×1024 pixels), termed BS-LDM. This framework employs a conditional latent diffusion model to generate high-resolution soft tissue images with fine detail and critical lung pathology by performing bone suppression in the latent space. We implement offset noise during the noise addition phase of the training process to better render low-frequency information in soft tissue images. Additionally, we introduce a dynamic clipping strategy during the sampling process to refine pixel intensity in the generated soft tissue images. We compiled a substantial and high-quality bone suppression dataset, SZCH-X-Rays, including high-resolution paired CXR and DES soft tissue images from 818 patients, collected from our partner hospitals. Moreover, we pre-processed 241 pairs of CXR and DES soft tissue images from the JSRT dataset, the largest publicly available dataset. Comprehensive experimental and clinical evaluations demonstrate that BS-LDM exhibits superior bone suppression capabilities, highlighting its significant clinical potential.

1 Introduction

Morbidity and mortality rates associated with lung disease have remained high in recent years. Chest X-Rays (CXRs) are a widely accepted low-dose technique for lung screening. While Computed Tomography (CT) offers greater accuracy, it is associated with significantly higher radiation doses. Consequently, CXRs are generally the preferred method. However, even skilled interpreters can overlook lesions in lung areas that are not prominent, mainly because 75% of the lung area in CXRs overlaps with bone, hindering disease detection and diagnosis. To improve interpreta-

tion accuracy, bone suppression techniques have been introduced. The most highly regarded method currently in use is Dual-Energy Subtraction (DES) imaging. This technique uses multiple radiographs taken at different X-ray energy levels, which are then merged to produce a bone-suppressed image. Nevertheless, this method requires expensive equipment and exposes patients to higher radiation doses. Therefore, researchers are striving to develop less harmful, cost-effective bone suppression techniques.

Recently, diffusion models (Ho, Jain, and Abbeel 2020) have emerged as a novel class of generative models capable of synthesizing high-quality images, addressing the challenges of mode collapse and convergence issues commonly associated with Generative Adversarial Networks (GANs). Among these, Latent Diffusion Models (LDMs) (Rombach et al. 2022) enable high-resolution image synthesis by compressing data into the latent space for computation. Building on these advancements, to the best of our knowledge, we introduce the first end-to-end LDM-based framework for bone suppression in high-resolution CXR images (1024×1024 pixels), termed BS-LDM. High-resolution medical images not only counteract blurriness but also advance the resolution to clinically relevant levels (Weber et al. 2023). Our framework employs a conditional LDM to generate high-resolution soft tissue images, preserving fine details and critical lung pathology by performing bone suppression in the latent space. To enhance the rendering of low-frequency information in soft tissue images, we incorporate offset noise during the noise addition phase of the training process (Guttenberg 2023). Additionally, we introduce a dynamic clipping strategy during sampling to refine pixel intensity in the generated images. In addition, we compiled a high-quality bone suppression dataset named SZCH-X-Rays, consisting of high-resolution paired CXR and DES soft tissue images from 818 patients, collected from partner hospitals. Furthermore, we processed 241 pairs of CXR and DES soft tissue images from the JSRT dataset, the largest open-source dataset for bone suppression currently available (Shiraishi et al. 2000). We performed operations such as inversion and contrast adjustment to restore these images to conventional radiographs. Our proposed network reliably generates soft tissue images with high bone suppression rates while preserving fine image details and critical lung lesions. Our primary contributions are summarized as follows:

1) We developed an innovative end-to-end conditional LDM, BS-LDM, designed for bone suppression in high-resolution CXR images (1024×1024 pixels). This model aids in the clinical diagnosis of lung diseases such as inflammation, tuberculosis, and masses or nodules.

2) We demonstrated the effectiveness of offset noise in generating low-frequency information in soft tissue images. Additionally, we introduced a dynamic clipping strategy to enhance the pixel intensity of the generated images.

3) We compiled a substantial and high-quality bone suppression dataset named SZCH-X-Rays, consisting of high-resolution paired CXR and DES soft tissue images from 818 patients gathered from partner hospitals. Moreover, we pre-processed and publicized 241 pairs of CXR and DES soft tissue images from the JSRT dataset.

2 Related Work

Traditional bone suppression methods considered it as a regression prediction problem, using supervised techniques. Suzuki *et al.* (Suzuki et al. 2006) employed a multi-task artificial neural network to generate bone images from CXRs, which could then be subtracted to produce soft-tissue-like images. However, the small dataset size limited its generalizability. Subsequently, statistical analysis methods emerged to identify and eliminate bony structures using image features in an unsupervised manner. Simkó *et al.* (Simkó et al. 2009) proposed a clavicle suppression algorithm that created a bone image from a gradient map adjusted along the bone boundary. This bone image was then subtracted from the CXRs to produce soft tissue images. Juhasz *et al.* (Juhasz et al. 2010) employed the active shape model to segment anatomical structures in CXRs and suppress bone shadows. They applied this model to the JSRT dataset, which remains the only publicly available dataset of its kind. In general, statistical-based methods require accurate segmentation and boundary annotations, which often lack high-level semantic information about bony structures.

Recently, various bone suppression methodologies have utilized deep learning algorithms to generate soft tissue images. These methods either treat bone suppression as an end-to-end image denoising task or focus on predicting the bone residual (Rani et al. 2022). Yang *et al.* (Yang et al. 2017) designed a cascaded multi-scale Convolutional Neural Network (CNN) trained within the gradient domain of CXRs for bone suppression. Although the model achieved impressive performance, it failed to maintain high levels of perceptual and structural integrity. In another study, Gusarev *et al.* (Gusarev et al. 2017) conceptualized bones as noise by utilizing combined features of an autoencoder and a deep CNN to remove bone structures, which unfortunately resulted in image blurring. Drawing inspiration from GAN (Goodfellow et al. 2014), Zhou *et al.* (Zhou et al. 2019) introduced a Multi-scale Conditional Adversarial Network (MCA-Net) designed to produce soft tissue images while preserving essential anatomical structures. To avoid the problem of inconsistent background intensity in gradient-based methods, Chen *et al.* (Chen et al. 2019) introduced a cascaded CNN into the wavelet domain. Rajaraman *et al.* (Rajaraman et al. 2021) developed the ResNet-BS model to suppress bones

in CXRs, validating its utility through subsequent analytic tasks. Additionally, Liu *et al.* (Liu et al. 2023) presented a bone suppression technique for lateral CXRs using a data rectification method and a distillation learning algorithm. Chen *et al.* (Chen et al. 2023) proposed BS-Diff, which entails the development of a conditional diffusion model in the pixel space augmented by an enhancement module. However, this model exhibited limitations in resolution, fine details, and computational demands. Despite these advancements, existing models frequently encounter challenges such as compromised visual quality, excessive computational requirements, loss of spatial and textural details, and inability to adequately preserve lung lesions.

3 Method

3.1 Overall Architecture

In this section, we introduce our proposed BS-LDM framework for bone suppression, which predicts high-resolution and high-quality soft tissue images, as illustrated in Fig. 1. This model employs a conditional LDM approach to generate detailed soft tissue images while preserving critical lung pathology by performing bone suppression in the latent space. Our BS-LDM utilizes the U-Net (Ronneberger, Fischer, and Brox 2015) as the noise estimator network, with CXR latent variables serving as conditional input via channel concatenation. To facilitate efficient processing, we use the Vector Quantized GAN (VQGAN) (Esser, Rombach, and Ommer 2021) to transform input data into a lower-dimensional latent space. This transformation significantly reduces the computational demands of generating high-resolution images, enabling BS-LDM to produce soft tissue images with high bone suppression rates while retaining fine image details. Additionally, we incorporate offset noise during the training process and a dynamic clipping strategy during sampling. These enhancements are specifically designed to improve the reproduction of low-frequency information within the soft tissue images, resulting in a more accurate depiction of underlying anatomical structures.

3.2 Conditional Latent Diffusion Models

Latent diffusion models, exemplified by stable diffusion (Rombach et al. 2022), operate through a forward and reverse process. In contrast to conventional diffusion models like Denoising Diffusion Probabilistic Models (DDPMs) (Ho, Jain, and Abbeel 2020), LDMs significantly reduce the computational load for generating high-resolution images by encoding data into a compressed latent space. Specifically, for an image $x \in \mathbb{R}^{C \times H \times W}$, the encoder ε transforms x into a latent variable $z = \varepsilon(x)$.

During the forward process, random Gaussian noise is incrementally introduced to the latent representations of the original images until the final distribution approximates Gaussian noise. In conditional LDMs, conditions are added to guide the diffusion trajectory. The approximate posterior for this process can be denoted by $q_{\theta}(z_{1:T}|z_0)$, as given in Eqs. 1 and 2:

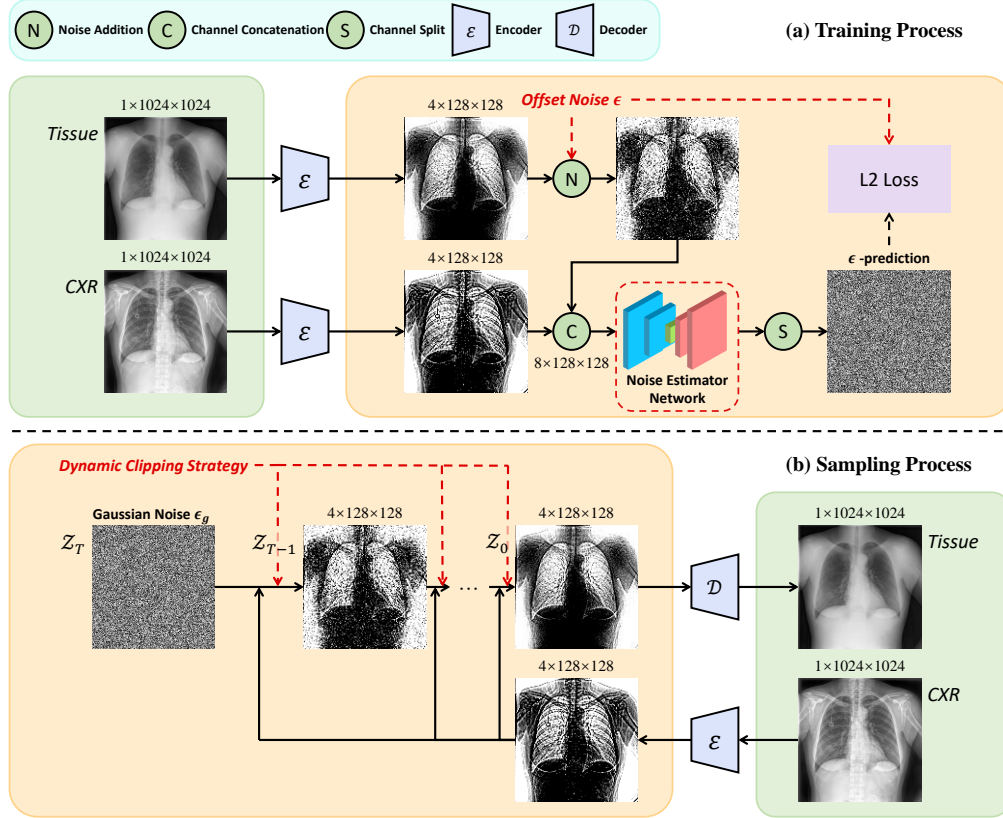


Figure 1: Overview of the proposed BS-LDM. The top side of the framework describes the training process of BS-LDM, where the latent variables of the CXR images are used as conditional guidance for the estimation of the offset noise. At the bottom, the sampling process of BS-LDM is detailed, where the latent variables obtained after each sampling step are dynamically clipped to ensure that the resulting pixel intensities are consistent with real soft tissue images.

$$q_{\theta}(z_{1:T}|z_0) = \prod_{t=1}^T q_{\theta}(z_t|z_{t-1}, \tilde{z}), \quad (1)$$

$$q(z_t|z_{t-1}, \tilde{z}) = \mathcal{N}(z_t; \sqrt{1 - \beta_t}(z_{t-1}, \tilde{z}), \beta_t I), \quad (2)$$

where β_t adjusts the mean and variance of the noise added at each step, with \tilde{z} representing the imposed condition.

During the reverse process, the model retraces the noise addition steps to revert to the distribution of the original images. This reversal relies on the model’s ability to predict the noise characteristics learned during the forward process. In conditional LDMs, the generation process is influenced by specific conditions which guide the forward diffusion trajectory. This process can be denoted by $p_{\theta}(z_{0:T}|\tilde{z})$, as described in Eqs. 3 and 4:

$$p_{\theta}(z_{0:T}|\tilde{z}) = p(z_T) \prod_{t=1}^T p_{\theta}(z_{t-1}|z_t, \tilde{z}), \quad (3)$$

$$p_{\theta}(z_t|z_{t-1}, \tilde{z}) = \mathcal{N}(z_{t-1}; \mu_{\theta}(z_t, t, \tilde{z}), \Sigma_{\theta}(z_t, t, \tilde{z})), \quad (4)$$

where the parameters μ_{θ} and Σ_{θ} are estimated by a network based on the U-Net architecture.

3.3 Offset Noise

In the forward process of diffusion models, each pixel incrementally accumulates a small quantity of independently and identically distributed Gaussian noise at every step. The model is trained to predict this noise after the original image has been perturbed. However, we observe that low-frequency features are more resistant to corruption by Gaussian noise, as shown in Fig. 2. This resistance means that the low-frequency information of the original image may not be entirely erased during the forward process, resulting in noise that differs somewhat from pure Gaussian noise. In contrast, the reverse process begins with Gaussian noise, creating a discrepancy between the forward and reverse processes. As a consequence, the low-frequency information in the synthesized image tends to resemble Gaussian noise more than the original image. This can lead to a bias in the mean value of generated soft tissue images, causing luminance inconsistencies and poorer readability.

To address this issue, we introduce offset noise ϵ during the forward process. This involves adding an additional bias noise to the standard noise addition procedure, as illustrated in Fig. 3 and formalized in Eq. 5:

$$\epsilon \sim \mathcal{N}(0, I + \lambda \cdot \Sigma), \quad (5)$$

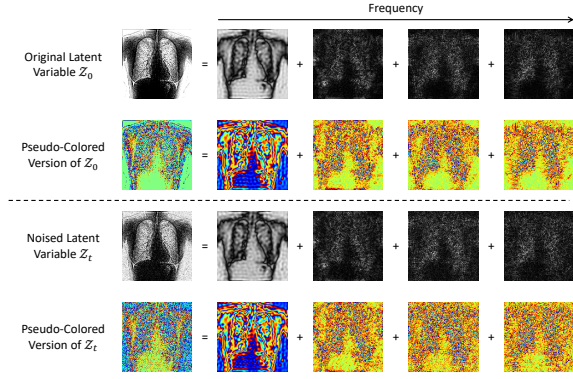


Figure 2: Visualization of high- and low-frequency feature decomposition of latent variables before and after Gaussian noise addition.

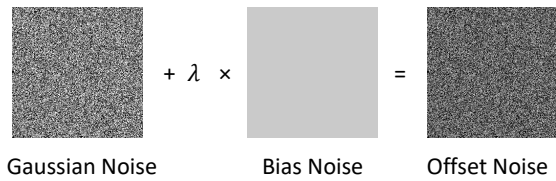


Figure 3: Illustration of the composition of offset noise.

where Σ is a covariance matrix of all ones, and λ is the weight of the bias noise, typically set to 0.1. Bias noise can be understood as zero-frequency noise, which can be obtained from one-dimensional Gaussian noise through tensor broadcasting. The purpose of introducing offset noise is to completely destroy the low-frequency information of the original images during the noise addition process, ensuring the endpoints converge to true Gaussian noise. This approach enhances the resemblance of the generated images to real images by broadening the spectrum of pixel intensity variations.

3.4 Dynamic Clipping Strategy

In the reverse process of diffusion models, constraining the predicted values of x to the range $[-1, 1]$ ensures numerical stability. This technique, previously employed in the literature (Ho, Jain, and Abbeel 2020) but not widely discussed, was termed "static thresholding" by Saharia *et al.* (Saharia *et al.* 2022). To address the pixel saturation problem common in classifier-free guidance (Ho and Salimans 2022), Saharia *et al.* proposed "dynamic thresholding." This method involves setting s to a specific percentile of absolute pixel values, clipping data to $[-s, s]$ if $s > 1$, and then normalizing by s to stop pixel saturation by pushing the data inwards.

Typically, thresholding is not used in LDMs (Lu *et al.* 2022). However, we observed that without thresholding, the LDM in our task suffers from pixel saturation, leading to excessive contrast in the generated results. While static thresholding provides numerical stability and mitigates pixel saturation, it significantly limits the variance of generated images. This causes an accumulation of extreme pixel values

and a noticeable luminance difference between generated and real images. Dynamic thresholding, although an improvement, also carries the risk of causing the contrast of the generated images to be significantly lower than that of the real images when applied to LDMs, and does not satisfy the practical needs of generating high-quality soft tissue images.

To address these issues, we propose a dynamic clipping strategy where the clipping interval $[-s, s]$ is determined by the current sampling step t . We use a linear function to describe the relationship between the clip threshold s and the sampling step t , as shown in Eq. 6:

$$s = \omega \cdot t + b, \quad (6)$$

where $\omega (> 0)$ represents the slope and $b (\geq 1)$ denotes the intercept of the linear function. By adjusting the clipping range from a more constrained to a broader span as the sampling process progresses, the dynamic clipping strategy provides the model with greater flexibility. This allows for a more nuanced adjustment of pixel intensities, ensuring that the contrast of the final synthesized images more closely matches that of the original images, which can be associated with improved readability of the generated soft tissue images and the corresponding diagnostic performance of the radiologists.

3.5 Encoder and Decoder

We utilize the encoder component of the VQGAN with a hybrid loss function to condense the pixel space $X \in \mathbb{R}^{1 \times H \times W}$ into a more compact latent space $X \in \mathbb{R}^{C \times \frac{H}{r} \times \frac{W}{r}}$, where r represents the compression factor, as illustrated in Fig. 1. Our VQGAN architecture consists of both an encoder and a decoder. After the conditional diffusion model completes its reverse process in the latent space, the decoder maps the latent representations back to the pixel space. During the training phase, the VQGAN network is trained to reconstruct CXR and DES soft tissue images. To balance computational efficiency and reconstruction fidelity, we chose $C = 4$ and $r = 8$ in our framework.

Hybrid Loss Function. In formulating the training objective for VQGAN, we employ a composite loss function that combines L1 loss \mathcal{L}_{L1} , quantization loss \mathcal{L}_{Qua} (Tudoiu *et al.* 2022), perceptual loss \mathcal{L}_{Per} (Johnson, Alahi, and Fei-Fei 2016), and adversarial loss \mathcal{L}_{Adv} from a patch-based discriminator, inspired by the Pix2PixHD framework (Wang *et al.* 2018). This multifaceted loss function aims to enhance the local realism of the reconstructed images and to avoid the blurring effects often linked with pixel-wise loss metrics such as L2 or L1 loss. The overall hybrid loss function is concisely formulated as Eq. 7:

$$\mathcal{L} = \lambda_{L1} \cdot \mathcal{L}_{L1} + \lambda_{Qua} \cdot \mathcal{L}_{Qua} + \lambda_{Per} \cdot \mathcal{L}_{Per} + \lambda_{Adv} \cdot \mathcal{L}_{Adv}, \quad (7)$$

where λ_{L1} , λ_{Qua} , λ_{Per} and λ_{Adv} are weights that balance the contributions of each component in the total loss.

4 Experiments and Results

4.1 Data Preprocessing

We compiled a dataset of 831 paired posterior-anterior CXR and DES soft tissue images, captured using a dual-exposure digital radiography system (Discovery XR656, GE Healthcare) from our partner hospitals. Originally archived in 14-bit DICOM format, the images were converted to PNG format for easier processing. Each image had dimensions of 2021×2021 pixels, with pixel sizes ranging up to 0.1943 mm. We excluded 13 image pairs due to operational errors, severe motion artifacts, and conditions like pleural effusions and pneumothorax, which could compromise analysis.

The refined dataset, named SZCH-X-Rays, comprised 818 image pairs. We divided this dataset into training, validation, and test sets in an 8:1:1 ratio. To enhance the alignment and integration of information between paired images, we applied image registration techniques. Additionally, we used contrast-limited adaptive histogram equalization to improve local contrast within the images.

We also processed 241 pairs of CXR and DES soft tissue images from the largest open-source dataset, JSRT. This involved operations such as inversion and contrast adjustment to restore them to conventional radiographs, supplementing our experimental dataset. For more efficient memory usage, all images from both the SZCH-X-Rays and JSRT datasets were resized to 1024×1024 pixels. Finally, the pixel values were normalized to the range $[-1, 1]$.

4.2 Implementation Details

All experiments were conducted using PyTorch 2.0.1 on a single Nvidia A100 80G GPU running on Ubuntu 20.04. We trained the VQGAN model from scratch for 1000 epochs with a batch size of 4, using the Adam optimizer (Kingma and Ba 2014). Similarly, our conditional diffusion model was trained from scratch for 2500 epochs with a batch size of 4, using the AdamW optimizer (Loshchilov and Hutter 2017), which took 22 hours. For VQGAN training, we configured the loss weights as follows: $\lambda_{L1} = \lambda_{Qaa} = 1$, $\lambda_{Per} = 0.001$, and $\lambda_{Adv} = 0.01$. This training process took 20 hours. We also employed an exponential moving average (EMA) strategy during the training of our conditional diffusion model, with an exponential decay coefficient set at 0.995. We instituted a dynamic learning rate schedule, starting with a learning rate of 0.0001 for the VQGAN generator, 0.0005 for the VQGAN discriminator, and 0.0002 for the conditional diffusion model. For the conditional diffusion model, we set the number of training and inference timesteps T to 1000. The variance schedule parameter β varied from 0.008 to 0.02, mapped across the T timesteps using a cosine noise schedule. In the reverse process, we implemented a dynamic clipping strategy with $\omega = 0.003$ and $b = 1.4$ as the slope and intercept of the linear function, respectively.

4.3 Comparison with the State-of-the-Arts

To ensure a fair evaluation, we benchmarked our proposed model against four state-of-the-art methodologies from recent literature: an autoencoder-based model (Gusarev et al. 2017), MCA-Net (Zhou et al. 2019), ResNet-BS (Rajaraman

et al. 2021), and BS-Diff (Chen et al. 2023). We utilized the default parameters provided in the open-source implementations of these competing methods and conducted experiments at the same resolution for consistency.

To assess the quality of the generated soft tissue images, we employed several evaluation metrics, including the Bone Suppression Ratio (BSR) (Hogeweg, Sánchez, and van Ginneken 2013), Mean Squared Error (MSE), Peak Signal-to-Noise Ratio (PSNR) (Hore and Ziou 2010), and Learned Perceptual Image Patch Similarity (LPIPS) (Zhang et al. 2018). Among these, BSR, MSE, and PSNR focus on pixel-level similarity, while LPIPS evaluates perceptual-level similarity.

The comparative performance of the various bone suppression techniques is detailed in Table 1 for the SZCH-X-Rays dataset and illustrated in Fig. 4 for the JSRT dataset. Results indicate that our method outperforms all other approaches across all metrics, producing soft tissue images with enhanced detail. On the SZCH-X-Rays dataset, the autoencoder-based model performed the poorest due to brightness differences and a significant loss of texture, while ResNet-BS and MCA-Net showed comparable results with slightly brighter central airways. Meanwhile, BS-Diff presented some texture blurring.

On the public JSRT dataset, the autoencoder-based model and MCA-Net were less effective in bone suppression compared to ResNet-BS and BS-Diff, which, though effective, lacked some intricate details.

4.4 Ablation Study

To ascertain the significance of offset noise and the dynamic clipping strategy within the framework of the BS-LDM, we conducted a series of experiments. These experiments involved training the model with and without using these components individually, using the SZCH-X-Rays and JSRT datasets. In scenarios where the dynamic clipping strategy was absent, we tested static thresholding, dynamic thresholding, and no clipping at all. Our results show that incorporating both offset noise and the dynamic clipping strategy is crucial for generating high-quality soft tissue images, as it allows for a more nuanced adjustment of low-frequency information. Furthermore, the dynamic clipping strategy proves to be feasible for the sampling process in latent diffusion models and demonstrates superiority over static and dynamic thresholding in our task. Quantitative evidence supporting these findings is presented in Table 2, with associated visualizations shown in Fig. 5.

4.5 Hyperparameter Analysis

To further investigate the effects of offset noise and the dynamic clipping strategy under varying hyperparameter settings, we conducted a hyperparameteric analysis for each dataset. The results, depicted in Fig. 6, indicate that for both datasets, the model performs optimally when the bias noise weight λ in the offset noise is set to 0.1, and the parameters ω and b are set to 0.003 and 1.4, respectively.

We observed that in offset noise, the value of λ significantly influences the model’s behavior, an excessively large λ can disrupt performance, while an excessively small λ has

Dataset	Method	BSR (\uparrow)	MSE (\downarrow)	PSNR (\uparrow)	LPIPS (\downarrow)
SZCH-X-Rays	Gusarev <i>et al.</i> (Gusarev et al. 2017)	0.944	0.0008	31.900	0.220
	MCA-Net (Zhou et al. 2019)	0.945	<u>0.0007</u>	<u>32.177</u>	0.118
	ResNet-BS (Rajaraman et al. 2021)	0.956	<u>0.0009</u>	<u>31.950</u>	<u>0.078</u>
	BS-Diff (Chen et al. 2023)	<u>0.971</u>	0.0008	31.057	0.191
	BS-LDM (Ours)	0.976	0.0006	32.224	0.051
JSRT	Gusarev <i>et al.</i> (Gusarev et al. 2017)	0.865	0.0009	31.216	0.193
	MCA-Net (Zhou et al. 2019)	0.892	0.0009	33.735	0.148
	ResNet-BS (Rajaraman et al. 2021)	<u>0.903</u>	0.0009	32.009	<u>0.139</u>
	BS-Diff (Chen et al. 2023)	0.902	<u>0.0008</u>	<u>33.937</u>	0.147
	BS-LDM (Ours)	0.908	0.0007	36.312	0.049

Table 1: Comparison on SZCH-X-Rays and JSRT datasets with the state-of-the-art methods using BSR, MSE, PSNR and LPIPS.

Offset Noise	Clipping	SZCH-X-Rays			JSRT		
		MSE (\downarrow)	PSNR (\uparrow)	LPIPS (\downarrow)	MSE (\downarrow)	PSNR (\uparrow)	LPIPS (\downarrow)
×	×	0.1131	30.054	0.553	0.2619	28.109	0.918
×	Static Thresholding	0.0164	30.222	0.141	0.0140	28.525	0.083
×	Dynamic Thresholding	0.0161	30.319	0.142	0.0123	29.368	0.081
×	Dynamic Clipping Strategy	<u>0.0080</u>	<u>31.557</u>	<u>0.053</u>	<u>0.0109</u>	<u>35.415</u>	<u>0.053</u>
✓	×	0.1105	30.056	0.549	0.2590	28.104	0.809
✓	Static Thresholding	0.0106	31.441	0.128	0.0140	28.525	0.083
✓	Dynamic Thresholding	0.0103	29.937	0.130	0.0153	29.040	0.072
✓	Dynamic Clipping Strategy	0.0006	32.224	0.051	0.0007	36.312	0.049

Table 2: Ablation performance on SZCH-X-Rays and JSRT datasets using MSE, PSNR and LPIPS.

Clinical Evaluation Criteria		Junior Radiologist	Intermediate Radiologist	Senior Radiologist
Lung vessel visibility	Clearly displayed (3)			
	Displayed (2)	2.431	2.858	2.984
	Not displayed (1)			
Airway visibility	Lobar and intermediate bronchi (3)			
	Main bronchus and rump (2)	2.561	2.643	2.937
	Trachea (1)			
Degree of bone suppression	Nearly perfect suppression (3)			
	Unsuppressed bones less than 5 (2)	2.781	2.793	2.722
	5 or more bones unsuppressed (1)			

Table 3: Image quality assessment of BS-LDM scored by three radiologists with 6, 11 and 20 years of experience, respectively.

Junior Radiologist	Precision (\uparrow)	Recall (\uparrow)	F1 Score (\uparrow)
CXR	0.70	0.40	0.51
Soft tissue	0.73	0.56	0.63
Senior Radiologist	Precision (\uparrow)	Recall (\uparrow)	F1 Score (\uparrow)
CXR	0.74	0.51	0.60
Soft tissue	0.75	0.75	0.75

Table 4: Diagnostic utility assessment of BS-LDM calculated from the diagnostic results of two radiologists with 6 and 11 years of experience, respectively.

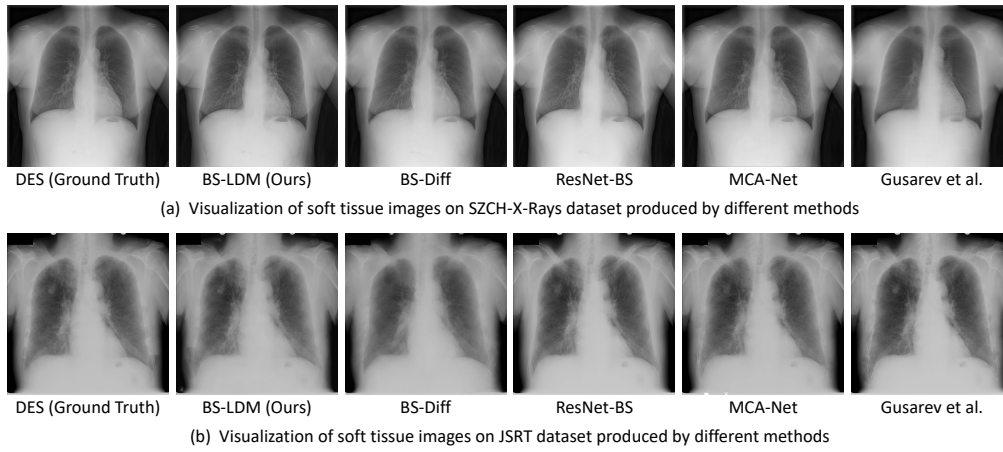


Figure 4: Visualization of soft tissue images on SZCH-X-Rays and JSRT datasets produced by different methods.

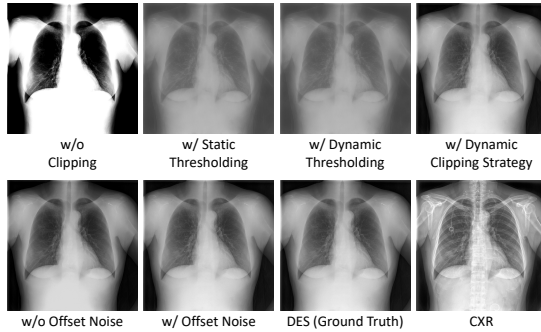


Figure 5: Visualization of ablation studies of offset noise and the dynamic clipping strategy of BS-LDM.

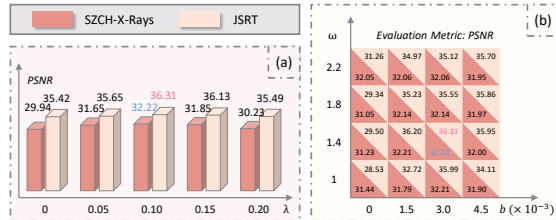


Figure 6: Visualization of hyperparameter analysis of offset noise (a) and the dynamic clipping strategy (b) on SZCH-X-Rays and JSRT datasets.

minimal impact. For the dynamic clipping strategy, the parameters ω and b are somewhat dependent on the data characteristics, with extreme values potentially leading to performance degradation.

4.6 Clinical Evaluation

Image quality assessment. The soft tissue images generated by BS-LDM on the SZCH-X-Rays dataset were independently evaluated for image quality based on established clinical criteria (Bae et al. 2022; Hong et al. 2021) widely used to assess bone suppression efficacy. Three radiologists,

with 6, 11, and 20 years of experience, respectively, conducted these evaluations at our partner hospitals. The detailed results are presented in Table 3. The average scores for lung vessel visibility, airway visibility, and degree of bone suppression were 2.758, 2.714, and 2.765, respectively, on a scale where the maximum score was 3. These results indicate that our BS-LDM not only effectively suppresses bones but also retains fine details and lung pathology.

Diagnostic utility assessment. The diagnostic value of soft tissue imaging was independently evaluated by two radiologists with 6 and 11 years of experience, respectively, following the X-ray diagnostic standard (Bansal and Beese 2019). For this analysis, we used the SZCH-X-Rays dataset, which included confirmed lesions through computed tomography, covering common lung diseases such as inflammation, tuberculosis, and masses or nodules.

Among the 818 data pairs assessed, 79 pairs contained one or more of these lesions. The radiologists independently evaluated both the conventional CXRs and the soft tissue images generated by our model. The results of these evaluations are summarized in Table 4, which highlights key metrics such as Precision, Recall, and the F1 Score. The findings indicate that the soft tissue images produced by BS-LDM enable radiologists to diagnose lesions more thoroughly and accurately than conventional CXRs, thereby validating the high clinical diagnostic value of our model.

5 Conclusion

To enhance the precision and completeness of lesion detection by radiologists, we propose BS-LDM, a conditional latent diffusion model designed for bone suppression in high-resolution CXR images. During the training and sampling processes, we incorporate offset noise and a dynamic clipping strategy to improve the reproduction of low-frequency information. Our model excels at generating soft tissue images with high bone suppression while retaining critical details and preserving lung lesion integrity. Rigorous experimental and clinical evaluations confirm the exceptional bone suppression performance and significant clinical utility of

BS-LDM. However, challenges remain, including reducing sampling steps and time, eliminating motion artifacts, and integrating our model with downstream tasks. Future work will focus on addressing these issues to advance the field of medical image analysis.

References

- Bae, K.; Oh, D. Y.; Yun, I. D.; and Jeon, K. N. 2022. Bone suppression on chest radiographs for pulmonary nodule detection: comparison between a generative adversarial network and dual-energy subtraction. *Korean Journal of Radiology*, 23(1): 139.
- Bansal, T.; and Beese, R. 2019. Interpreting a chest X-ray. *British Journal of Hospital Medicine*, 80(5): C75–C79.
- Chen, Y.; Gou, X.; Feng, X.; Liu, Y.; Qin, G.; Feng, Q.; Yang, W.; and Chen, W. 2019. Bone suppression of chest radiographs with cascaded convolutional networks in wavelet domain. *IEEE Access*, 7: 8346–8357.
- Chen, Z.; Sun, Y.; Qin, W.; Ge, R.; Pan, C.; Deng, W.; Liu, Z.; Min, W.; Elazab, A.; Wan, X.; et al. 2023. BS-Diff: Effective Bone Suppression Using Conditional Diffusion Models from Chest X-Ray Images. *arXiv preprint arXiv:2311.15328*.
- Esser, P.; Rombach, R.; and Ommer, B. 2021. Taming transformers for high-resolution image synthesis. In *Proceedings of the IEEE/CVF Conference on Computer Vision and Pattern Recognition*, 12873–12883.
- Goodfellow, I.; Pouget-Abadie, J.; Mirza, M.; Xu, B.; Warde-Farley, D.; Ozair, S.; Courville, A.; and Bengio, Y. 2014. Generative adversarial nets. *Advances in Neural Information Processing Systems*, 27.
- Gusarev, M.; Kuleev, R.; Khan, A.; Rivera, A. R.; and Khatkhat, A. M. 2017. Deep learning models for bone suppression in chest radiographs. In *2017 IEEE Conference on Computational Intelligence in Bioinformatics and Computational Biology (CIBCB)*, 1–7. IEEE.
- Guttenberg, N. 2023. Diffusion with offset noise. <https://www.crosslabs.org/blog/diffusion-with-offset-noise>.
- Ho, J.; Jain, A.; and Abbeel, P. 2020. Denoising diffusion probabilistic models. *Advances in Neural Information Processing Systems*, 33: 6840–6851.
- Ho, J.; and Salimans, T. 2022. Classifier-free diffusion guidance. *arXiv preprint arXiv:2207.12598*.
- Hogeweg, L.; Sánchez, C. I.; and van Ginneken, B. 2013. Suppression of translucent elongated structures: applications in chest radiography. *IEEE Transactions on Medical Imaging*, 32(11): 2099–2113.
- Hong, G.-S.; Do, K.-H.; Son, A.-Y.; Jo, K.-W.; Kim, K. P.; Yun, J.; and Lee, C. W. 2021. Value of bone suppression software in chest radiographs for improving image quality and reducing radiation dose. *European Radiology*, 31: 5160–5171.
- Hore, A.; and Ziou, D. 2010. Image quality metrics: PSNR vs. SSIM. In *2010 20th International Conference on Pattern Recognition*, 2366–2369. IEEE.
- Johnson, J.; Alahi, A.; and Fei-Fei, L. 2016. Perceptual losses for real-time style transfer and super-resolution. In *Computer Vision—ECCV 2016: 14th European Conference, Amsterdam, The Netherlands, October 11–14, 2016, Proceedings, Part II 14*, 694–711. Springer.
- Juhász, S.; Horváth, Á.; Nikházy, L.; Horváth, G.; and Horváth, Á. 2010. Segmentation of anatomical structures on chest radiographs. In *XII Mediterranean Conference on Medical and Biological Engineering and Computing 2010: May 27–30, 2010 Chalkidiki, Greece*, 359–362. Springer.
- Kingma, D. P.; and Ba, J. 2014. Adam: A method for stochastic optimization. *arXiv preprint arXiv:1412.6980*.
- Liu, Y.; Zeng, F.; Ma, M.; Zheng, B.; Yun, Z.; Qin, G.; Yang, W.; and Feng, Q. 2023. Bone suppression of lateral chest x-rays with imperfect and limited dual-energy subtraction images. *Computerized Medical Imaging and Graphics*, 105: 102186.
- Loshchilov, I.; and Hutter, F. 2017. Decoupled weight decay regularization. *arXiv preprint arXiv:1711.05101*.
- Lu, C.; Zhou, Y.; Bao, F.; Chen, J.; Li, C.; and Zhu, J. 2022. Dpm-solver: A fast ode solver for diffusion probabilistic model sampling in around 10 steps. *Advances in Neural Information Processing Systems*, 35: 5775–5787.
- Rajaraman, S.; Zamzmi, G.; Folio, L.; Alderson, P.; and Antani, S. 2021. Chest X-ray bone suppression for improving classification of tuberculosis-consistent findings. *Diagnostics*, 11(5): 840.
- Rani, G.; Misra, A.; Dhaka, V. S.; Zumpano, E.; and Vocaturo, E. 2022. Spatial feature and resolution maximization GAN for bone suppression in chest radiographs. *Computer Methods and Programs in Biomedicine*, 224: 107024.
- Rombach, R.; Blattmann, A.; Lorenz, D.; Esser, P.; and Ommer, B. 2022. High-resolution image synthesis with latent diffusion models. In *Proceedings of the IEEE/CVF Conference on Computer Vision and Pattern Recognition*, 10684–10695.
- Ronneberger, O.; Fischer, P.; and Brox, T. 2015. U-net: Convolutional networks for biomedical image segmentation. In *Medical Image Computing and Computer-Assisted Intervention—MICCAI 2015: 18th International Conference, Munich, Germany, October 5–9, 2015, Proceedings, Part III 18*, 234–241. Springer.
- Saharia, C.; Chan, W.; Saxena, S.; Li, L.; Whang, J.; Denton, E. L.; Ghasemipour, K.; Gontijo Lopes, R.; Karagol Ayan, B.; Salimans, T.; et al. 2022. Photorealistic text-to-image diffusion models with deep language understanding. *Advances in Neural Information Processing Systems*, 35: 36479–36494.
- Shiraishi, J.; Katsuragawa, S.; Ikezoe, J.; Matsumoto, T.; Kobayashi, T.; Komatsu, K.-i.; Matsui, M.; Fujita, H.; Kodera, Y.; and Doi, K. 2000. Development of a digital image database for chest radiographs with and without a lung nodule: receiver operating characteristic analysis of radiologists’ detection of pulmonary nodules. *American Journal of Roentgenology*, 174(1): 71–74.

- Simkó, G.; Orbán, G.; Máday, P.; and Horváth, G. 2009. Elimination of clavicle shadows to help automatic lung nodule detection on chest radiographs. In *4th European Conference of the International Federation for Medical and Biological Engineering: ECIFMBE 2008 23–27 November 2008 Antwerp, Belgium*, 488–491. Springer.
- Suzuki, K.; Abe, H.; MacMahon, H.; and Doi, K. 2006. Image-processing technique for suppressing ribs in chest radiographs by means of massive training artificial neural network (MTANN). *IEEE Transactions on Medical Imaging*, 25(4): 406–416.
- Tudosiu, P.-D.; Pinaya, W. H. L.; Graham, M. S.; Borges, P.; Fernandez, V.; Yang, D.; Appleyard, J.; Novati, G.; Mehra, D.; Vella, M.; et al. 2022. Morphology-Preserving Autoregressive 3D Generative Modelling of the Brain. In *International Workshop on Simulation and Synthesis in Medical Imaging*, 66–78. Springer.
- Wang, T.-C.; Liu, M.-Y.; Zhu, J.-Y.; Tao, A.; Kautz, J.; and Catanzaro, B. 2018. High-Resolution Image Synthesis and Semantic Manipulation with Conditional GANs. In *Proceedings of the IEEE Conference on Computer Vision and Pattern Recognition*.
- Weber, T.; Ingrisch, M.; Bischl, B.; and Rügamer, D. 2023. Cascaded latent diffusion models for high-resolution chest x-ray synthesis. In *Pacific-Asia Conference on Knowledge Discovery and Data Mining*, 180–191. Springer.
- Yang, W.; Chen, Y.; Liu, Y.; Zhong, L.; Qin, G.; Lu, Z.; Feng, Q.; and Chen, W. 2017. Cascade of multi-scale convolutional neural networks for bone suppression of chest radiographs in gradient domain. *Medical Image Analysis*, 35: 421–433.
- Zhang, R.; Isola, P.; Efros, A. A.; Shechtman, E.; and Wang, O. 2018. The unreasonable effectiveness of deep features as a perceptual metric. In *Proceedings of the IEEE Conference On Computer Vision and Pattern Recognition*, 586–595.
- Zhou, B.; Lin, X.; Eck, B.; Hou, J.; and Wilson, D. 2019. Generation of virtual dual energy images from standard single-shot radiographs using multi-scale and conditional adversarial network. In *Computer Vision—ACCV 2018: 14th Asian Conference on Computer Vision, Perth, Australia, December 2–6, 2018, Revised Selected Papers, Part I 14*, 298–313. Springer.